Energy & Environmental Science

Deconvolution of Intermixed Redox Processes in Ni-based Cation-Disordered Li-Excess Cathodes

Journal:	*Energy & Environmental Science*
Manuscript ID	EE-ART-11-2020-003526.R1
Article Type:	Paper
Date Submitted by the Author:	20-Jan-2021
Complete List of Authors:	Huang, Tzu-Yang; University of California Berkeley, Department of Chemical and Biomolecular Engineering; Lawrence Berkeley National Laboratory, Energy Storage and Distributed Resources Division Crafton, Matthew; University of California Berkeley, Department of Chemical and Biomolecular Engineering; Lawrence Berkeley National Laboratory, Energy Storage and Distributed Resources Division Yuan, Yue; E O Lawrence Berkeley National Laboratory, Energy Storage and Distributed Resources Tong, Wei; Lawrence Berkeley National Laboratory, Energy Storage and Distributed Resources McCloskey, Bryan; University of California Berkeley, Department of Chemical and Biomolecular Engineering; E O Lawrence Berkeley National Laboratory, Energy Storage and Distributed Resources Division

PAPER

Deconvolution of Intermixed Redox Processes in Ni-based Cation-Disordered Li-Excess Cathodes

Received 00th January 20xx,
Accepted 00th January 20xx

DOI: 10.1039/x0xx00000x

Tzu-Yang Huang, [ab] Matthew J. Crafton, [ab] Yuan Yue, [b] Wei Tong, [b] and Bryan D. McCloskey [*ab]

Cation-disordered rock-salt transition-metal oxides and oxyfluorides (DRX) have emerged as promising cathode materials for Li-ion batteries due to their potential to reach high energy densities and accommodate diverse, lower cost transition-metal chemistries compared to conventional layered oxide materials. However, the intricate local coordination environment in DRX also results in complex electrochemical electron transfer involving parallel mechanisms of transition-metal (TM) redox and oxygen (anionic) redox. Without decoupled and quantitative information of these intermixed redox processes, the origin of irreversibility, voltage hysteresis, and capacity fading is obscured, impeding the development of strategies to address these issues. Here we deconvolute the mixed redox processes in a Ni-based DRX, $Li_{1.15}Ni_{0.45}Ti_{0.3}Mo_{0.1}O_{1.85}F_{0.15}$, by combining ^{18}O isotopic enrichment, differential electrochemical mass spectrometry (DEMS), and *ex-situ* acid titration. The summation of TM-redox and oxygen-redox capacities measured through our approach agrees with the net electron transfer measured by the potentiostat. This study reveals much less Ni oxidation efficiency (59.5%) than its initially designed efficiency (100%) due to competition of oxygen redox, which can occur at potentials as low as 4.1 V (vs. Li/Li^+). We propose that the chemical approach presented in this work and its future extension can resolve and quantify various mixed redox processes in different DRX, which allows clear correlations among material design, deconvoluted redox capacities, and battery performance.

Table of contents entry

Capacity deconvolution of intermixed high-valent Ni redox and oxygen redox through ^{18}O labelling, acid titration, and mass spectrometry

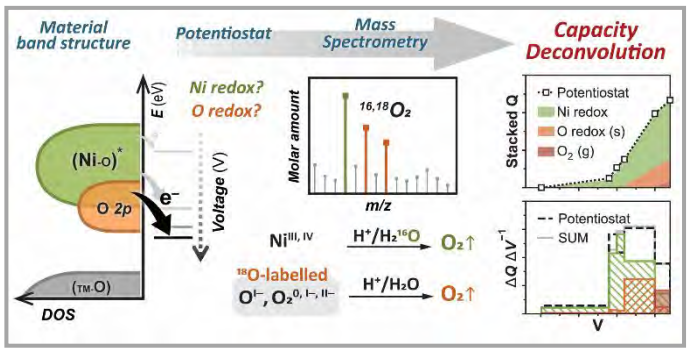

Broader context

Coexistence of both high-valent transition metal redox and oxygen (anionic) redox is a prevailing phenomenon in Li-excess cathode materials that can potentially push Li-ion batteries towards higher capacities and energy densities for powering future electric vehicles. The distribution of each redox component in the operating voltage window is directly linked to the rechargeable battery performance and energy efficiency. Therefore, decoupling their contributions quantitatively is vital to engineer emerging Li-excess cathode materials for practical applications. During the charging process, high-valent transition metal and oxidized oxygen species can competitively form in similar voltage range, which makes it particularly challenging to use existing techniques to resolve each redox capacity quantitatively. In this work, we provide an unique way to quantify and distinguish high-valent nickel and oxidized oxygen species through a combination of analytical tools that allow us to fully deconvolute the interwoven redox process even in an intricate cation-disordered Li-excess cathode material.

[a.] *Department of Chemical and Biomolecular Engineering, University of California–Berkeley, Berkeley, California 94720, USA. E-mail: bmcclosk@berkeley.edu*
[b.] *Energy Storage and Distributed Resources Division, Lawrence Berkeley National Laboratory, Berkeley, California 94720, USA.*
† Electronic Supplementary Information (ESI) available:
See DOI: 10.1039/x0xx00000x

Introduction

Improving the limited energy density and lowering the cost of traditional cathode materials in Li-ion batteries has become increasingly crucial with the surging demands from portable-electronic and electric-vehicle markets. New cathode chemistries such as cation-disordered rock-salt transition-metal oxides or oxyfluorides (DRX)[1–6] have gained considerable attention due to their potential in outperforming conventional layered lithium-intercalation chemistry. Sufficient lithium excess in DRX materials can facilitate lithium-ion diffusion and percolation through lattice tetrahedral holes having low energy barriers.[1,2] In certain compositions, over 0.7 Li per unit formula ($Li_{1+x}TM_{1-x}O_{2-y}F_y$, where TM represents transition metal and $0 < x, y < 1$) are electrochemically accessible, which leads to exceptionally high capacity that can surpass 300 mAh g^{-1}.[3–5] Even though some Li-excess layered oxides have shown comparable capacity, they typically require one of the following constraints: 1) specific transition-metal chemistry (TM = [Mn, Co, Ni] or Ir in $Li_{1+x}TM_{1-x}O_2$);[6–9] 2) specific Li-excess extent (x = 1/3, 2/3 in $Li_{1+x}TM_{1-x}O_2$ which are equivalent to Li_2TMO_3, Li_5TMO_6).[10–13] On the other hand, the limitation to form a stable layered structure is relaxed for DRX materials. Accommodating various transition metal ions into the DRX lattice with a variable Li-excess range not only enlarges the domain of design and optimization, but also enhances the feasibility of cobalt-free cathode materials and therefore avoids the consequential cost of using cobalt.[6,14,15] Thus, DRX materials' capability of reaching a high energy density, increasing design flexibility, and reducing cost makes it a prominent candidate for next-generation cathodes in Li-ion batteries.

However, the diverse metal-oxide (or metal-oxyfluoride) chemistry in the DRX lattice also leads to a complex local coordination environment[16–18] and further obscures underlying redox processes. First, the inherent cation-mixing and Li-excess nature of the DRX material has been argued as the major cause of non-bonding O *2p* orbitals at a higher energy level than analogous bonding TM–O bands.[19] Second, various extents of frontier-orbital interelectronic repulsion (Mott-Hubbard splitting)[13,20] and octahedral distortion (Jahn-Teller effect)[21,22] were suggested to level down a portion of split anti-bonding TM–O bands with predominant TM character. Arising from the two prerequisites described above, overlapping of the lowered TM-dominated band and the elevated O-dominated band results in parallel mechanisms of transition-metal redox and oxygen redox,[13,19,20,23] which is atypical in Li-stoichiometric layered materials (x = 0 in $Li_{1+x}TM_{1-x}O_2$). While X-ray[24–31] and magnetic-resonance[10] spectroscopic research has elucidated TM redox and oxygen redox in structurally ordered oxides, few studies can successfully resolve and quantify each redox process's contribution to capacity individually. Most cathode materials lacking a proper standard reference spectrum require data-driven principal component analysis[32] or simplified coordination models[25] to best-fit the ratio of oxidized TM, but materials with varying indistinct local coordination, such as that induced by severe cation migration,[27] could obscure the exact TM formal valences of the selected spectral components. Similarly, numerical fitting with the aid of capacity (regressand, the dependent variable in regression analysis) in the voltage profile is typically required to obtain parameters that translate spectroscopic shape[32] or intensity[30] (regressor, the independent variable in regression analysis) into oxygen redox capacity. Non-arbitrary assignment of spectrum peak ranges and positions that represent the oxidized oxygen could be challenging due to strong adjacent peaks and background signals. As a result, direct counting of electrochemical electron transfer from spectroscopic information remains hard to achieve, especially for DRX materials with extremely diverse and intricate short-range structure.

In light of these challenges, this work combines isotopic enrichment, *ex-situ* acid titrations, and mass spectrometry (TiMS) to deconvolute the interwoven transition-metal and oxygen redox processes in a DRX cathode. This combination allows accurate quantification of various gas molecules released from distinguishable reactions when the charged (delithiated) DRX material is etched and dissolved by strong acid. The well-defined stoichiometry of H^+-participating outgassing reactions facilitates unambiguous backcalculation of the electrochemical capacity contributed from solid-state TM redox and oxygen redox, respectively. Moreover, *in-situ* differential electrochemical mass spectrometry (DEMS) monitors and quantifies oxygen redox involving irreversible gaseous O_2 loss that is usually not captured by other approaches. Adding each component capacity of the various redox processes measured using our analytical techniques matches the net electron transfer measured by the potentiostat, with a difference of less than 10 mAh g^{-1} at any given potential. From these measurements, we reveal that oxygen redox in DRX can occur in parallel with TM redox above the potential as low as 4.1 V (vs. Li/Li^+). The competition of intermixed redox processes leads to much lower TM oxidation efficiency (~60%) than its hypothetical value (100%), with which the DRX was initially designed. As new DRX material designs are considered, we anticipate these techniques and results to be valuable to probe the various intermixed redox processes described above to optimize charge compensation reversibility.

Methodology

Material synthesis and characterization

The Ni-based DRX material, $Li_{1.15}Ni_{0.45}Ti_{0.3}Mo_{0.1}O_{1.85}F_{0.15}$ (NTMF), was synthesized by following a conventional solid-state annealing method similar to that in a previous study.[33] Precursors of Li_2CO_3, $NiCO_3$, TiO_2, MoO_2 and LiF were mixed stoichiometrically through high energy milling for 3 h. Mixed precursors were then annealed at 700 °C for 10 h in air. Powder X-ray diffraction was performed on a Bruker D2-Phaser with Cu Kα radiation.

Isotopic enrichment

NTMF powders were enriched with ^{18}O by adopting and modifying the method developed in our previous studies.[34–36] Briefly, an as-prepared NTMF sample is heated to 600 °C under

a 97 at% $^{18}O_2$ in N_2 environment for 6 h (**Error! Reference source not found.**a). A full description of procedures and oxygen balance analysis can be found in the Electronic Supplementary Information (ESI)† Note S1.

Electrochemical cell assembly

Modified Swagelok-type cells[37,38] as depicted in Fig. S3a were used for electrochemical measurements and *in-situ* outgassing monitoring. Each cell is highly leak-tight by sealing two stainless-steel tubular current collectors against a quartz tube envelope (13 mm ID × 15 mm OD, 25 mm length) with compressed O-rings (Markez FFKM perfluoroelastomer, Marco Rubber & Plastics). Two capillaries (0.0625 inch OD, VICI) as the gas inlet and outlet were hard soldered into the top current collector. To create a headspace for the evolved gas, a stainless-steel ring spacer (1 mm height) was placed over the cathode disk. Cathodes were made under Ar atmosphere by casting slurry comprising 70 wt% active material, 20 wt% conductive carbon (Super P, TIMCAL), 10 wt% polyvinylidene fluoride (Solef 6010/1001, SOLVAY), and N-Methyl-2-pyrrolidone solvent (anhydrous, 99.5%, Sigma Aldrich) onto stainless-steel meshes of 12 mm diameter. The cathodes were dried overnight under static vacuum at 120 °C in a heated antechamber attached to the glove box. The loading density of active materials ranged from 7 to 10 mg cm^{-2}. Lithium disks of 11 mm diameter cut from Li foil (FMC) were used as anodes. For each cell, a polypropylene separator (Celgard 2500) facing the cathode and a QM-A quartz microfiber filter (Whatman) facing the anode, each 12 mm diameter, were used as separators with 80 µL of 1 M $LiPF_6$ (Gotion) in EC/DEC (BASF, 1:1 v/v) as the electrolyte. The separators were arranged not only to avoid shorting the battery during assembly and disassembly, but also to reduce the amount of residual quartz microfiber adhered to the cathode for extraction.[35,36,39,40] All cells were assembled in the glove box.

Differential electrochemical mass spectrometry

The differential electrochemical mass spectrometry (DEMS) instrument was custom-built and operated as described in our previous publications.[37,38] The setup is calibrated for O_2 (research grade, PRAXAIR) and CO_2 (> 99.9%, PRAXAIR) in N_2 carrier gas (ultra-high purity, PRAXAIR). The headspace of all DEMS cells was purged and replaced by N_2 before electrochemical measurements to remove the interference of ^{36}Ar isotope on the mass-spectrometry detection of double-tagged $^{18,18}O_2$ evolution. To allow each NTMF particle in the porous electrode to achieve similar state of charge, each DEMS cell was charged at a constant current rate of 0.1 Li^+ h^{-1} (29.5 mA g^{-1}) to a certain cut-off voltage and subsequently held at the cut-off voltage, unless otherwise noted, until the current rate dropped to 0.01 Li^+ h^{-1} (2.95 mA g^{-1}), which was controlled by a Bio-Logic VSP-series potentiostat. Accumulated gas in each cell was purged intermittently using 500 µL pulses of N_2 every 10 minutes at recorded gas pressures and room temperatures. Swept-out gas was subsequently sent to a holding chamber, where it was leaked to a mass-spectrometry chamber for analysis.

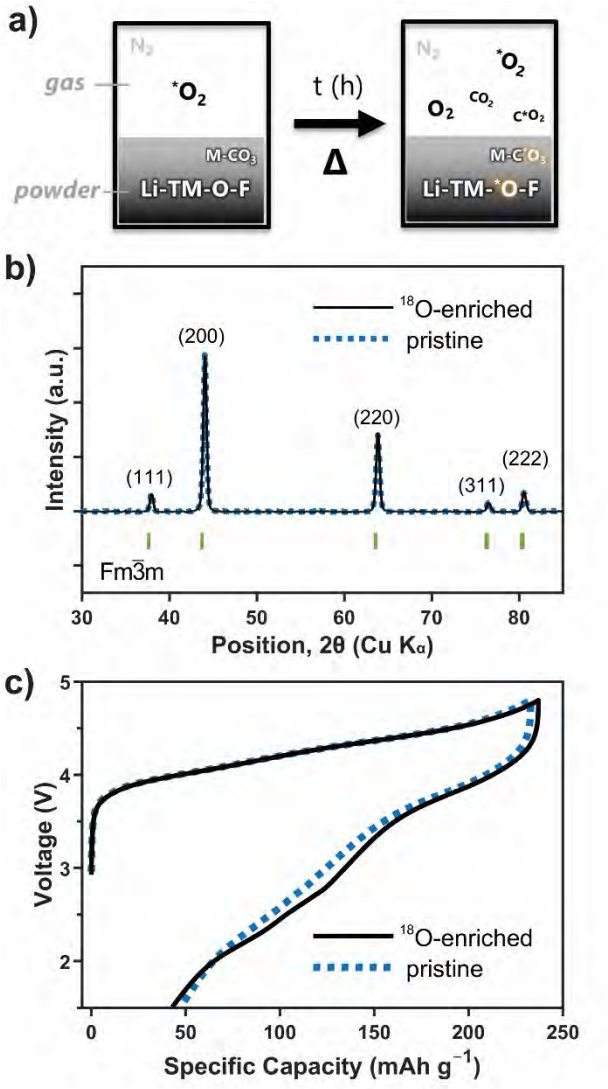

Fig. 1 Characterization of $Li_{1.15}Ni_{0.45}Ti_{0.3}Mo_{0.1}O_{1.85}F_{0.15}$ (NTMF) before and after isotopic enrichment. (a) Illustration of isotopic exchange process. Both NTMF (denoted as Li-TM-O-F) lattice and surface native carbonate (NACN, denoted as M-CO_3) are labelled with ^{18}O at the end of the process. Star symbols indicate partial ^{18}O enrichment. (b) X-ray diffraction patterns of NTMF before (blue dotted line) and after (black line) ^{18}O-enrichment. Green vertical bars denote Bragg diffraction peak positions calculated by using the $Fm\bar{3}m$ space group, lattice parameter a = 4.14146 Å,[33] and Cu Kα radiation. (c) First-cycle voltage profiles of pristine (blue dotted line) and ^{18}O-enriched (black line) NTMF at a rate of 0.1 Li^+ h^{-1} without holding at the 4.8 V switching voltage, showing no substantial change in bulk redox chemistry after isotopic enrichment.

Titration mass spectrometry

Each titration glass vessel was custom-made from two tubular reservoirs connected through both an O-ring-sealed (H_2SO_4-resistant Viton fluoroelastomer) polytetrafluoroethylene stop-cock and a gas channel, so that the solid sample and liquid titrant were stored separately with shared headspace before mixing (titration), as depicted in Fig. S3b. Charged cathodes were extracted from DEMS cells in the glove box, rinsed with 1 mL diethyl carbonate (DEC, BASF) for three times, and dried at room temperature under vacuum for > 3 h to remove

residual electrolyte. For each titration experiment, either weighed NTMF powder or an extracted cathode was sealed into the titration glass vessel in the glove box. Concentrated sulfuric acid (10 M H_2SO_4 (aq), Sigma Aldrich) was prepared as the titrant to efficiently supply excess amount of H^+ (aq) that avoids isotopic exchange of evolved gases with H_2O,[35] while sulphate ions remain stable and inert during the titration. Titration mass spectrometry (TiMS) was operated using a similar setup as DEMS, but with a titration vessel in place of a modified Swagelok cell.[41] The headspace of the glass vessel was purged and replaced with N_2 carrier gas (ultra-high purity, PRAXAIR) after injection of N_2-sparged 10 M H_2SO_4. The gas composition inside the glass vessel was monitored by the mass spectrometer to ensure that residual air, especially any O_2 potentially introduced during the injection, was thoroughly removed before opening the stopcock to mix the sample with H_2SO_4 (aq). Gas released from H^+-participating reactions in each titration vessel was purged by 2 mL of pulsed N_2 every 2 minutes at recorded gas pressures and room temperatures. Swept-out gas was subsequently analyzed by the mass spectrometer.

Results and discussion

^{18}O isotopic enrichment on Ni-based DRX powder

In this study, we will be monitoring gas evolution from DRX materials in operational batteries and during their immersion in aqueous acid solutions. Because the same gas species could originate from either the DRX active material or its surrounding liquid environment (e.g., electrolyte degradation and oxidation of surface carbonate impurities both contribute to CO_2 evolution in batteries), distinguishing among mixed gas evolution sources and reactions is clearly important. To decouple these various contributions, we first implemented ^{18}O isotopic enrichment on a model Ni-based DRX material, $Li_{1.15}Ni_{0.45}Ti_{0.3}Mo_{0.1}O_{1.85}F_{0.15}$ (NTMF). The as-synthesized NTMF powder, without any detectable impurity phases as confirmed using X-ray powder diffraction (XRD, Fig. 1b), was placed in a sealed tube with a known quantity of ^{18}O-containing (97 at%) O_2 in the headspace and was heated to facilitate oxygen isotopic exchange (**Error! Reference source not found.**a). Previous studies have shown both surface native carbonate, which invariably remains after synthesis and handling of oxide cathode materials, and the transition-metal oxide lattice oxygen can be partially enriched with ^{18}O through the as-described method, where isotopic compositions and enrichment level of carbonate were measured by strong acid titration afterwards.[35] Titrating ^{18}O-enriched surface residual carbonate specified that it had a 39.9 mol% ^{18}O enrichment ($^{18}O/(^{16}O + {}^{18}O)$) with an almost uniform binomial distribution, indicating uniform enrichment of the carbonate throughout the NTMF material (Table S1). By analyzing the tube headspace composition after the labelling procedure with mass spectrometry, the bulk mean ^{18}O enrichment within the NTMF lattice is estimated to be 11.7 mol%, excluding surface carbonate. Detailed enrichment processes and calculations are described in the ESI† Note S1. Of note, the overall ^{18}O enrichment level in the NTMF is higher than that in Ni-Mn-Co layered oxides (3%–7%) following similar procedures,[34] which implies faster oxygen exchange kinetics for NTMF than the conventional layered oxides. We further performed XRD and electrochemical tests to verify if the heating process impacts the nature of NTMF. As shown in Fig. 1b, no substantial difference in XRD patterns was observed, which means that the extended rock-salt phase persists after isotopic enrichment. In addition, nearly identical first-cycle voltage profiles (Fig. 1c) between the enriched and as-received NTMF suggest no significant alterations in dominant redox mechanisms. The structural and electrochemical invariance thus justifies that the NTMF bulk redox chemistry is very likely unaffected by the ^{18}O-enrichment procedure.

In-situ monitoring of outgassing reactions

Gas release during electrochemical operation is a crucial indicator of both irreversible oxygen evolution and deleterious cathode-electrolyte interactions. To quantitatively analyze outgassing, we performed DEMS with ^{18}O-enriched NTMF as the cathode material. Fig. 2a shows a representative result obtained from DEMS analysis of ^{18}O-enriched NTMF, which provides the charging profile of a NTMF cathode along with O_2 evolution rates during a constant-rate (0.1 Li^+ h^{-1}, 29.5 mA g^{-1}) charge followed by a voltage hold at 4.8 V vs. Li/Li^+. We observe that the O_2 evolution onset potential is around 4.5 V, in accord with our previous study.[33] DEMS further discloses the distribution among $^{16,16}O_2$, $^{16,18}O_2$, and $^{18,18}O_2$ evolution. The onset potential of the three isotopic O_2 species is identical (Fig. S1a) and suggests no kinetic isotope effect as well as similar electrochemical origins for each of the O_2 isotopes, which is lattice oxygen redox that results in irreversible gaseous O_2 loss. **Error! Reference source not found.** compares the cumulative isotopic O_2 compositions evolved from three distinct electrodes charged to various cut-off voltages as well as the solid-state bulk mean ^{18}O enrichment calculated from the post-enrichment tube headspace oxygen balance. The overall amount of O_2 evolved is useful to backcalculate quantitative capacity contributions (reasonably assuming 4 electrons per O_2 loss), which will be addressed in the last part of the discussion.

As shown in **Error! Reference source not found.**, the distribution among isotopic O_2 species remains similar at cut-off voltages from 4.6 V to 4.8 V, while net ^{18}O enrichment in O_2 loss decreases slightly and approaches the lattice bulk mean value as the cut-off voltage increases. This result implies that near the onset potential, O_2 loss begins from the NTMF crystal surface where solid-state ^{18}O enrichment is expected to be higher than the core.[34] The higher enrichment extent near the surface of the

Table 1 Isotopic distribution of *in-situ* O_2 loss and its ^{18}O enrichment

Cut-off Voltages (V)	Distribution (%)			Enrichment	O_2 loss [a]
	$^{16,16}O_2$	$^{16,18}O_2$	$^{18,18}O_2$	^{18}O (%)	(mmol mol^{-1})
4.6	77.7	19.4	2.9	12.6	5.9
4.7	78.0	19.2	2.8	12.4	14.0
4.8	78.3	18.9	2.8	12.2	26.0
Bulk [b]				11.7	

[a] Amount normalized to the net mole of active material, NTMF;
[b] Lattice bulk mean value obtained from the enrichment process.

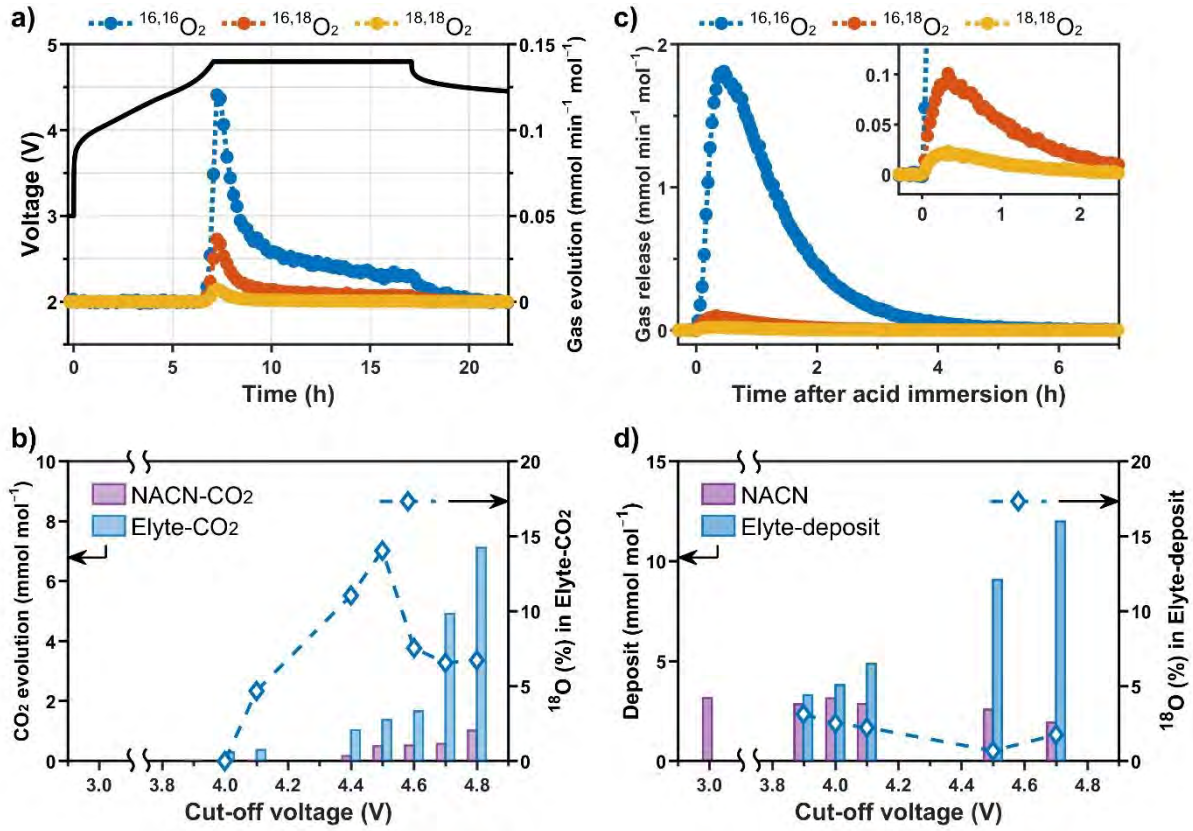

Fig. 2 *In-situ* gas evolution (DEMS) and *ex-situ* acid titration (TiMS) of NTMF. (a) Voltage profile (black line) and isotopic O_2-loss rates (solid circles) for ^{18}O-enriched NTMF charged at 0.1 Li^+ h^{-1} (29.5 mA g^{-1}) to 4.8 V (vs. Li/Li^+), subsequently held at 4.8 V until the current rate dropped to 0.01 Li^+ h^{-1} (2.95 mA g^{-1}) and allowed to rest at open circuit after the voltage hold. (b) Cumulative CO_2 evolution from native-carbonate decomposition (NACN-CO_2, plum bars) and electrolyte degradation (Elyte-CO_2, blue bars), obtained from DEMS. Blue hollow markers indicate ^{18}O content in Elyte-CO_2, suggesting surface reactivity of NTMF. (c) Isotopic O_2-release rates for the extracted 4.5 V-cathode titrated by 10 M H_2SO_4. Zoomed inset displays $^{16,18}O_2$ and $^{18,18}O_2$ release at a lower order of magnitude than untagged O_2. (d) Amount of native carbonate (NACN, plum bars) and carbonate-like solid deposits from electrolyte degradation (Elyte-deposit, blue bars), quantified by TiMS. Uncharged cathode is shown at the average open circuit voltage, 3.0 V, during the rest period before charge. Blue hollow markers indicate ^{18}O content in the Elyte-deposit. All quantities of gases and surface deposits are normalized to the net mole of active material, NTMF.

NTMF particle likely arises from the nature of our isotopic enrichment process, during which exposure time, temperature, and lattice-oxygen-exchange kinetics should result in a radial enrichment gradient near the surface. Converting differential isotopic O_2 evolution rates into ^{18}O enrichment along the voltage profile (Fig. S1b) further shows a higher ^{18}O enrichment level near the gaseous O_2 onset than at higher states of charge (≈ lattice bulk mean value). Nevertheless, the initial deviation of ^{18}O enrichment in evolved O_2 compared to the solid-state bulk mean ^{18}O enrichment value is particularly small (**Error! Reference source not found.**). Notice that cumulative O_2 loss is < 3% of total lattice oxygen even at the high cut-off voltage (4.8 V) hold. Given these results, it is clear that the bulk mean ^{18}O enrichment calculated from the oxygen balance accurately describes the overall solid-state enrichment level within the NTMF crystal even though a near surface radial gradient exists.

CO_2 outgassing monitored *in-situ* by DEMS provides integral information to track surface reactivity and its resulting parasitic reactions. Because the NTMF surface native carbonate (NACN) is ^{18}O-enriched, we can utilize the quantitative distribution among gaseous $C^{16,16}O_2$, $C^{16,18}O_2$, and $C^{18,18}O_2$ to decouple different contributions during electrochemical operation. Previous studies have ruled out conductive carbon in TM-oxide composite cathodes as the carbon source for CO_2 evolution[42] and accordingly have reasoned that double-tagged $C^{18,18}O_2$ predominantly evolves from NACN decomposition.[35,36] Therefore, combining $C^{18,18}O_2$ outgassing DEMS data with the known solid-state isotopic distribution in NACN allows quantification of CO_2 originating directly from NACN oxidation,[43] while the rest of the CO_2 is evolved from electrolyte degradation (Table S2). The bar graph in Fig. 2b depicts cumulative CO_2 arising from NACN oxidation (NACN-CO_2) and electrolyte degradation (Elyte-CO_2), respectively, on NTMF-cathodes charged to various cut-off voltages. With a cut-off voltage of 3.9 V, no significant CO_2 evolution was observed. The amount of Elyte-CO_2 gradually increases as the cut-off voltage is increased from 4.0 V to 4.6 V, while NACN-CO_2 evolution begins at a relatively higher voltage (4.4 V). When the cathode's potential surpasses 4.6 V, cumulative Elyte-CO_2 rises dramatically, more than twofold, which signals the onset of pronounced electrolyte degradation.

In addition, we observe ^{18}O integrated into CO_2 that evolves from electrolyte degradation (Fig. 2b), indicating that reactive oxygen species originating from either NACN or NTMF lattice oxidation can contribute to electrolyte degradation. The line graph in Fig. 2b further displays the ^{18}O enrichment in Elyte-CO_2

as a measure to evaluate the extent of cathode (NACN or lattice oxidation)-induced electrolyte degradation. By increasing the cut-off voltage from 4.0 V to 4.5 V, the ^{18}O content in Elyte-CO_2 increases from 0% to 14%, which suggests escalating parasitic reactions between the electrolyte and species originating from NACN or oxide oxidation. Below 4.5 V, we expect that the origin for this ^{18}O integration is predominantly from reactive oxygen species emanating from NACN given the following explanation. It is highly likely that one of the oxygen atoms in Elyte-CO_2 originated from the electrolyte solvent molecules[35,36] (which contains essentially no ^{18}O), so we expect at most ~ 6% ^{18}O content (half of NTMF lattice enrichment, ~12%) in Elyte-CO_2 if we assumed that all ^{18}O originates from the NTMF lattice. In fact, we observed 14% ^{18}O in Elyte-CO_2 at 4.5 V, more than double the ^{18}O possible if it originated from the NTMF lattice. Given these results, it is clear that reactive oxygen species released from the direct oxidation of NACN,[43] with 39.9% ^{18}O enrichment, has to contribute significantly to electrolyte degradation and subsequent Elyte-CO_2 outgassing at voltages $\leq$ 4.5 V. A considerable drop of the ^{18}O enrichment in Elyte-CO_2 occurs with a cut-off voltage $\geq$ 4.6 V and is likely due to the competition of disparate electrolyte degradation processes. With the probable mechanism described previously for electrolyte solvent degradation, the 6%–7% ^{18}O content in Elyte-CO_2 above 4.6 V implies that reactive oxidized oxygen species released from NTMF lattice (e.g., reactive superoxo, peroxo, or singlet oxygen) reacts with the electrolyte solvent, and is therefore likely to be the predominant source of ^{18}O in Elyte-CO_2 at cut-off voltages $\geq$ 4.6 V.

Ex-situ titration mass spectrometry

Surface carbonates. Mixtures of residual NACN (carbonates that inevitably remain after material synthesis and transfer in air) and interface parasitic reaction products form surface carbonates during electrochemical operation. *Ex-situ* acid titration (denoted as TiMS) decomposes carbonate-like species to release CO_2.[34–36] By adopting isotopic analysis similar to that of *in-situ* CO_2 outgassing, TiMS can decouple NACN and electrolyte-originating carbonate deposits (denoted as Elyte-deposit) quantitatively. As shown in the bar graph of Fig. 2d, the amount of NACN decreases moderately as the cut-off voltage increases, which is complementary to the gradual increase of *in-situ* NACN-CO_2 outgassing measured during battery charge (Fig. 2b). Adding up the quantity of residual NACN and NACN-CO_2 at each cut-off voltage corresponds to the initial quantity of solid-state NACN (at open-circuit voltage, OCV ≈ 3.0 V), which implies that *in-situ* degradation of NACN leads to CO_2 outgassing directly in a stoichiometric amount. On the other hand, the Elyte-deposit grows much more drastically than the NACN diminishes. The growing Elyte-deposit is likely to cover both NACN and NTMF lattice surface, which can be one carbon source for Elyte-CO_2 outgassing (Fig. 2b). The line graph of Fig. 2d displays low ^{18}O content < 5% in Elyte-deposit and exhibits no substantial variation across the voltage window, which suggests electrolyte solvent as the predominant oxygen source of carbonate-like Elyte-deposits.

Lattice oxidized species. To identify various oxidized species that form during charge, we exploit their instability and subsequent characteristic gas emission in an acidic environment. As will be shown, analyzing the mixture of gases evolved from a charged NTMF-electrode immersed in strong acid with mass spectrometry facilitates quantification of oxidized components, both the transition metal and lattice oxygen oxidation, within the NTMF bulk. Previous studies have elucidated that lattice oxidized oxygen in layered oxides can disproportionate in acid and produce O_2.[35,40] In this work, we further extend the technique and discover that water splitting by oxidized Ni ions (Ni^{3+} or Ni^{4+}) that are dissolved from the NTMF lattice also leads to gaseous O_2 release during the acid titration. Fig. 2c presents one representative TiMS result with isotopic O_2 emission from a 4.5 V-cathode etched by 10 M H_2SO_4, which reveals that the amount of untagged O_2 ($^{16,16}O_2$) and tagged O_2 ($^{16,18}O_2$ + $^{18,18}O_2$) differs by over an order of magnitude. TiMS of the extracted cathode at a cut-off voltage as low as 3.9 V even displays prevailing $^{16,16}O_2$ release with almost no detectable ^{18}O-tagged O_2 species (Table S3). No O_2 emission is observed from an uncharged cathode immersed in acid. The significant deviation of TiMS results from the isotopic distribution of O_2 loss monitored *in-situ* by DEMS (Fig. 2a and Table 1) clearly indicates that at least two oxygen sources, including NTMF lattice oxidized oxygen, can contribute O_2 release during the acid titration. We verified H_2O as the additional source of oxygen by a control experiment, which swapped the initial ^{18}O-labelling conditions: titrating an untagged NTMF cathode with $H_2{}^{18}O$-containing H_2SO_4 solution. We ascribe this additional O_2 emission to water oxidation by oxidized nickel (Ni^{3+} or Ni^{4+}).

Known bulk mean ^{18}O enrichment within the solid-sate NTMF allows deconvolution of two different oxygen sources, depicted schematically in Fig. 3. Fig. **3** shows the NTMF particle surface immersed in acidic aqueous solution, where the dissolution and subsequent O_2-release reactions discussed below take place. Specifically, we assign all ^{18}O-tagged O_2 release to disproportionation of dissolved lattice oxidized

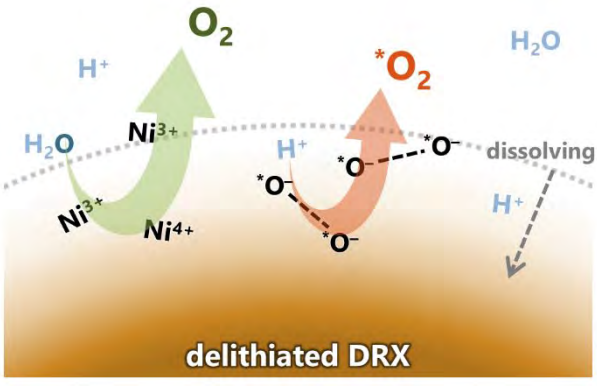

Fig. 3 Illustration of decoupled O_2-release reactions during the *ex-situ* acid titration of NTMF. Gray dotted curve outlines the acid-particle interface before dissolution. Star symbols indicate partial ^{18}O enrichment. Dissolved oxygen anions with formal valence of –1 (O^-) are displayed to represent all possible lattice oxidized oxygen species (ESI† Note S2). Other dissolved species, such as Li^+ and F^-, not participating in O_2-release reactions are not shown for clarity.

oxygen species whose net amount, including a portion of untagged $^{16,16}O_2$, can then be calculated given the total ^{18}O enrichment in the lattice. The remainder of the $^{16,16}O_2$ evolved accordingly determines the quantity of water splitting. See ESI† Note S3 for calculation details. Table S3 compares TiMS results of electrodes extracted at various cut-off voltages. Charged NTMF-cathodes exhibit O_2 emission from water splitting universally at all cut-off voltages above the initial OCV, while the disproportionation of NTMF-originating oxidized oxygen occurs significantly with cathodes charged above 4.1 V. TiMS of an uncharged NTMF cathode at OCV yields no detectable O_2 release, which indicates that TM species at their initial oxidation states, namely Ni^{2+}, Ti^{4+}, and Mo^{6+}, cannot induce water oxidation. Thus, we can exclude Ti^{4+} and Mo^{6+} from the water-splitting stoichiometry. It is noted that two factors could affect the accuracy of our isotopic analysis and deconvolution: 1) tagged H_2O produced from either NTMF lattice oxide dissolution or the disproportionation reaction; 2) natural abundance of ^{18}O in H_2O. However, H_2O molecules from the above two sources are present in much smaller quantities than untagged water in the acid solution. NTMF-originating $H_2{}^{18}O$ is at most, by assuming all lattice oxygen atoms form water molecules, 0.04% of H_2O in the acid solution (~8 mg NTMF in 2.5 mL 10 M H_2SO_4, density ≈ 1.55 g mL^{-1}). Natural abundance of ^{18}O is as low as 0.2%, which is two-orders-of-magnitude smaller than the bulk mean ^{18}O enrichment of the NTMF lattice. The impact of these two factors is clearly subtle and most likely insignificant, as implied by the particularly small amount of tagged O_2 release from cathodes extracted below 4.1 V (Table S3). Therefore, the as-described decoupling method can properly facilitate the following stoichiometric analysis with negligible interference.

Here we posit that during the acid titration, the dissolved oxidized oxygen species from NTMF lattice preferentially dimerize due to a close frontier-orbital energy and symmetry match, followed by disproportionation reaction, where star symbols denote partial ^{18}O enrichment:

$$2\left[{}^{*}\mathrm{O}\cdots{}^{*}\mathrm{O}\right]^{2-}+4\,\mathrm{H}^{+}\longrightarrow{}^{*}\mathrm{O}_2\uparrow+\,2\,\mathrm{H}_2{}^{*}\mathrm{O} \quad (1)$$

Meanwhile, oxidized Ni ions dissolved from NTMF lattice induce the water-splitting reaction, where n = 3 or 4:

$$4\,\mathrm{Ni}^{n+}+2(n-2)\,\mathrm{H_2O}\longrightarrow 4\,\mathrm{Ni}^{2+}+(n-2)\,\mathrm{O_2}\uparrow+\,4(n-2)\,\mathrm{H}^{+} \quad (2)$$

It is noted that different types of oxidized oxygen species could exist in the TM-oxide lattice.[10,44,45] However, the disproportionation reactions of various oxidized oxygen in the acid ultimately result in the same stoichiometry for backcalculation of O-redox capacity (see ESI† Note S2 for details). Thus, in Equation (1) and Fig. 3, we only show O^- as the model oxidized oxygen species for clarity. By adopting the stoichiometry in Equation (1), we can quantify lattice oxidized oxygen with the given amount of ^{18}O-enriched NTMF-originating O_2 release. With known moles of Ni in the titrated NTMF material and a measured quantity of O_2 originating from water-splitting, Equation (2) determines the average value of n (no O_2 release for n = 2), which can then be used to calculate electrochemical TM-redox capacity. We note that both Ni^{3+} and Ni^{4+} oxidize water and we unfortunately cannot distinguish between the two using TiMS. Also noteworthy is that while we can quantify transition metal redox using TiMS in NTMF materials, we did not observe transition metal-induced water-splitting in our previous studies on Ni-Mn-Co layered oxide materials.[35,40] The difference is likely due to the slow dissolution kinetics[33] and small water-oxidation driving force of Mn-containing oxides in the acidic aqueous environment, as suggested by comparing Pourbaix diagrams of two model Li-$Ni^{2+/3+}$-O materials containing Ti^{4+} and Mn^{4+}, respectively (Fig. S6).[46,47] See ESI† Note S4, Fig. S5, and Fig. S6 for detailed calculations and discussions about instability of TM-oxides in the aqueous environment.

Deconvolution of all electrochemical processes in the first charge

Individually quantified oxidized species in the NTMF allows direct accounting of each redox process's electrochemical capacity. Fig. **4**a presents average Ni oxidation state n, experimentally determined from TiMS analysis and Equation (2), as a function of extent of delithiation. At low states of charge (below 4.1 V), the experimental values closely follow a hypothetical diagonal line that assumes neither oxygen redox nor parasitic reactions, which suggests predominant Ni redox at low states of charge. The diminishing, but non-zero, slope implies competition of parallel redox processes at cut-off voltages surpassing 4.1 V. Average Ni oxidation states n > 3 suggest existence of Ni^{4+} in the NTMF during charge, which corresponds to the predictions from *ab initio* calculations.[18] Furthermore, the maximum n (~ 3.2) is far from 4, indicating limited utilization of Ni oxidation capability, namely a low Ni oxidation efficiency from Ni^{2+} ($(n-2)/(4-2)$ ≈ 60%). The highest average Ni oxidation state, particularly close to 3, agrees well with the estimation from X-ray absorption spectroscopy on the same NTMF and other similar series of DRX materials.[33,48] Above all, Ni redox capacities at various cut-off voltages can now be acquired through multiplying (n − 2) by the total moles of Ni in NTMF, as shown in Fig. 4b.

Oxygen redox arises as the second predominant redox mechanism in parallel with Ni redox at voltages above 4.1 V, as suggested by Fig. 4b that summarizes oxygen redox capacities involving either lattice oxidized oxygen species (Equation (1) and ESI† Note S2) or gaseous O_2 loss. The onset of lattice oxygen redox (4.1 V–4.5 V) concurs with escalating ^{18}O-enrichment level in Elyte-CO_2 outgassing (Fig. 2b), which implies that the participation of surface NTMF lattice-originating reactive oxidized oxygen species in electrolyte degradation cannot be ruled out. Overall, summation of each redox capacity (stacked area chart in Fig. 4c) lines up closely with the electrochemical capacity measured by the potentiostat (black dotted line in Fig. 4c), which validates our analytical approach. Because each charged electrode experienced a voltage hold that could sufficiently eliminate anyt kinetic effects, we expect that the relative contribution of redox processes shown here is close to its thermodynamic limit, as suggested by Table S4 and Fig. S4 which compare cathodes with various applied current during constant-rate charges. We note small discrepancies, particularly

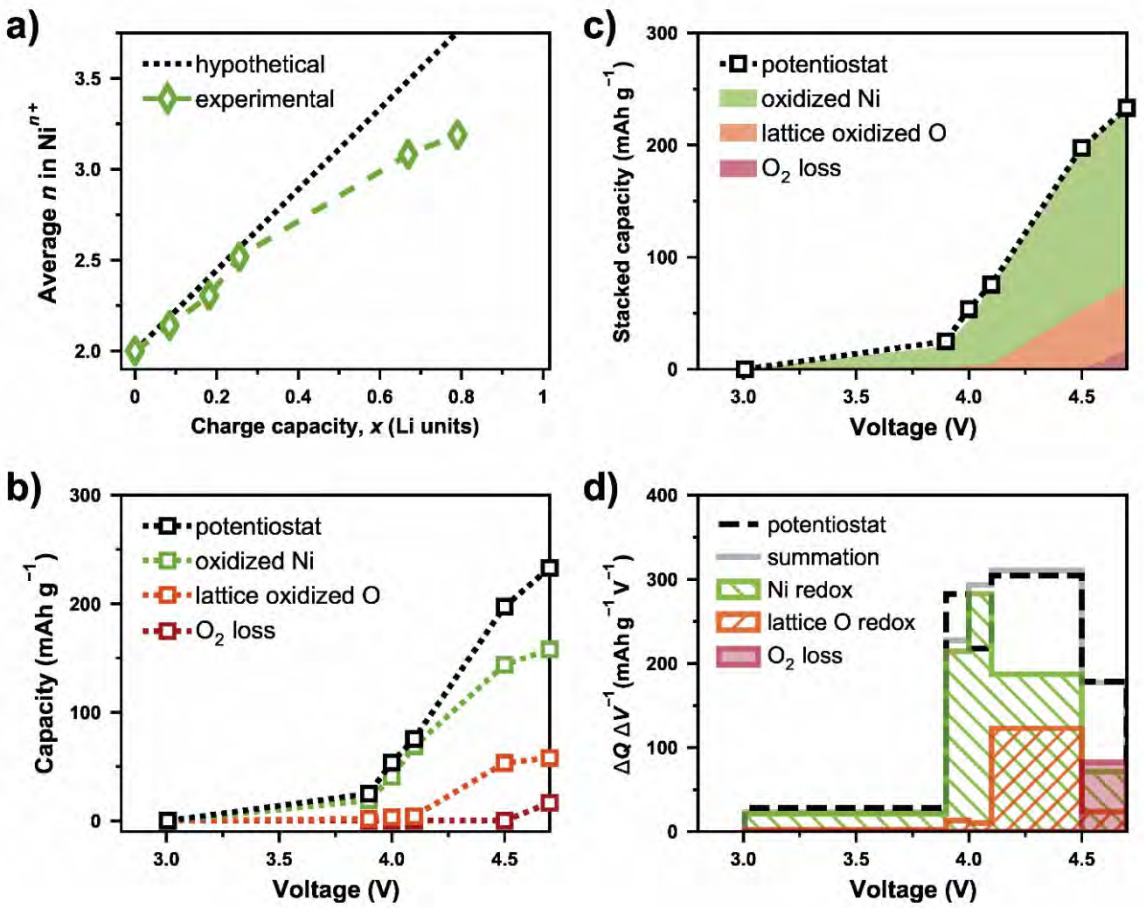

Fig. 4 Deconvolution of intermixed redox processes in NTMF. (a) Average Ni oxidation states in NTMF at various states of charge in Li units, x in $Li_{1.15-x}Ni_{0.45}Ti_{0.3}Mo_{0.1}O_{1.85}F_{0.15}$. The black dotted line represents the expected Ni oxidation state if only Ni redox, and no oxygen redox or parasitic side reactions, were to occur. (b) Cumulative charge capacity contributed by each individual redox process at different cut-off voltages. Black hollow markers denote electrochemical electron transfer to the current collector. (c) Stacked capacity of all individual decoupled redox components, compared to the potentiostat values. Colored areas denote the evolution and contribution of the corresponding constituents. (d) Differential capacity plot ($\Delta Q\,\Delta V^{-1}$) constructed from each individual redox capacity at various cut-off voltage. Gray line indicates summation of Ni-redox, lattice-O-redox, and O_2-loss contributions, compared to the differential capacity measured by the potentiostat.

in the 3.9 V–4.1 V range, between analytically and electrochemically measured capacities that may stem from interface parasitic reactions whose exact stoichiometry is challenging to define because of their intricate (electro)chemistry. With individual redox capacities at various cut-off voltages shown in Fig. 4b and c, we can re-construct a differential capacity ($dQ\,dV^{-1}$) plot based on each deconvoluted redox component, as shown in Fig. 4d. In a conventional differential capacity plot (Fig. S2), the asymmetry (non-Gaussian) and overlapping of redox peaks make it challenging to numerically deconvolute the predominant electrochemical processes. Here our differential capacity plot is useful to visualize and quantify the scale of each redox capacity contribution at any narrow voltage range within the cell's potential window. For example, 39.5% of the charge capacity is supplied by oxidizing oxygen between 4.1 V and 4.5 V. The formation and further oxidation of dimerized lattice oxygen atoms results in irreversible O_2 evolution, which accounts for 77.7% of net oxygen redox capacity (lattice oxidized oxygen + O_2 loss) at the high voltage ranging from 4.5 V to 4.7 V. Thus, even though data points of this current work are discretized, the $\Delta Q\,\Delta V^{-1}$ plot in Fig. 4d displays the potential of characterizing obscure DRX bulk redox processes in a clear and quantitative fashion using the analytical tools developed here.

Conclusions

Based on the deconvoluted charge capacity results, we propose that mixed *discharge* redox processes may also be resolved by applying the same analytical approach, which is currently under investigation and validation. With a clear distribution of various redox processes across the full-cycle voltage window, the first-cycle irreversibility and voltage hysteresis of DRX materials are better understood from each specific redox origin, which complements other techniques characterizing either short-range or long-range structural influence. For example, fluorination has been shown to not only impact the Li-percolating network, but also improve the cyclability of DRX materials.[49] As the authors reasoned that fluorine incorporation potentially increases the TM redox capacity by accommodating more low-valent TM, future studies are still needed to address how fluorination influences the TM oxidation efficiency, which

could also significantly alter the TM redox capacity as we have shown in this work. On the path towards cathodes with earth-abundant TM redox chemistry, namely Mn,[4–6,21,49] our analytical method requires further modifications because high-valent Mn (Mn^{3+} or Mn^{4+}) is inert in oxidizing water. Introducing another technique, such as iodometric titration,[41] may be suitable to quantify oxidized Mn species, but the slow reaction (or dissolution) kinetics of $Mn^{3+/4+}$-containing oxides in the aqueous solution may still need to be resolved in the future for achieving similar data throughput of this study.

In summary, this study presents a new route to characterize the intermixed redox mechanisms in Ni-based DRX materials. With ^{18}O-enrichment of the DRX lattice, high-valent Ni and oxidized oxygen species can be quantified separately by exploiting their instability that results in O_2-release in extreme acidic aqueous environments. The unambiguous and non-arbitrary stoichiometry allows accurate backcalculation of electrochemical capacity. Monitoring CO_2 outgassing and surface carbonate-like deposits reveals participation of reactive oxidized oxygen in the surface parasitic reactions, which accounts for a slight mismatch of capacity summation. Reconstructing the distribution of various redox processes as a function of cell voltage further discloses the overlapping nature of the DRX electronic band structure in a quantitative way. The proposed approach here can be useful to understand not only what factors affect TM oxidation efficiency/capacity but also which redox process dominates the irreversibility, voltage hysteresis and capacity loss over cycles/high rates in the context of designing and optimizing DRX materials for practical applications.

Author contributions

Conceptualization, T.-Y.H., M.J.C., and B.D.M.; Methodology, T.-Y.H., M.J.C., and B.D.M.; Investigation, T.-Y.H., M.J.C., and Y.Y.; Resources, Y.Y. and W.T.; Writing – Original Draft, T.-Y.H.; Writing – Review & Editing, T.-Y.H., M.J.C., Y.Y., W.T., and B.D.M.; Funding Acquisition, W.T. and B.D.M.; Supervision, W.T. and B.D.M.

Conflicts of interest

The authors declare no competing interests.

Acknowledgements

This research was supported by the Assistant Secretary for Energy Efficiency and Renewable Energy, Office of Vehicle Technologies of the U.S. Department of Energy under Contract No. DE-AC02-05CH11231. T.-Y.H. gratefully acknowledges support collectively from both Ministry of Education in Taiwan and UC Berkeley College of Chemistry through Taiwan Fellowship Program. The authors thank Jim Breen and Tom Adams for designing the titration glass vessels. The authors also thank Clintton Jessel and Douglas Scudder for making custom fittings used in the DEMS and TiMS measurements. T.-Y.H. thanks Joseph Papp, Dimitrios Fraggedakis, Zhengyan Lun, Zijian Cai, Huiwen Ji, and Minghao Zhang for insightful discussions.

Notes and references

1 J. Lee, A. Urban, X. Li, D. Su, G. Hautier and G. Ceder, *Science*, 2014, **343**, 519–522.

2 A. Urban, J. Lee and G. Ceder, *Advanced Energy Materials*, 2014, **4**, 1–9.

3 R. Chen, S. Ren, M. Knapp, D. Wang, R. Witter, M. Fichtner and H. Hahn, *Advanced Energy Materials*, 2015, **5**, 1–7.

4 N. Yabuuchi, M. Takeuchi, M. Nakayama, H. Shiiba, M. Ogawa, K. Nakayama, T. Ohta, D. Endo, T. Ozaki, T. Inamasu, K. Sato and S. Komaba, *Proceedings of the National Academy of Sciences of the United States of America*, 2015, **112**, 7650–5.

5 J. Lee, D. A. Kitchaev, D.-H. Kwon, C.-W. Lee, J. K. Papp, Y.-S. Liu, Z. Lun, R. J. Clément, T. Shi, B. D. McCloskey, J. Guo, M. Balasubramanian and G. Ceder, *Nature*, 2018, **556**, 185–190.

6 R. J. Clément, Z. Lun and G. Ceder, *Energy & Environmental Science*, 2020, **13**, 345–373.

7 S. Hy, H. Liu, M. Zhang, D. Qian, B. J. Hwang and Y. S. Meng, *Energy and Environmental Science*, 2016, **9**, 1931–1954.

8 P. K. Nayak, E. M. Erickson, F. Schipper, T. R. Penki, N. Munichandraiah, P. Adelhelm, H. Sclar, F. Amalraj, B. Markovsky and D. Aurbach, *Advanced Energy Materials*, 2018, **8**, 1–16.

9 A. J. Perez, Q. Jacquet, D. Batuk, A. Iadecola, M. Saubanère, G. Rousse, D. Larcher, H. Vezin, M. L. Doublet and J. M. Tarascon, *Nature Energy*, 2017, **2**, 954–962.

10 M. Sathiya, J. B. Leriche, E. Salager, D. Gourier, J. M. Tarascon and H. Vezin, *Nature Communications*, 2015, **6**, 1–7.

11 M. Sathiya, G. Rousse, K. Ramesha, C. P. Laisa, H. Vezin, M. T. Sougrati, M. L. Doublet, D. Foix, D. Gonbeau, W. Walker, A. S. Prakash, M. ben Hassine, L. Dupont and J. M. Tarascon, *Nature Materials*, 2013, **12**, 827–835.

12 G. van Tendeloo, E. J. Berg, J.-M. Tarascon, A. M. Abakumov, D. Foix, P. Novak, G. Rousse, R. Dominko, D. Gonbeau, M.-L. Doublet, M. Saubanere and E. McCalla, *Science*, 2015, **350**, 1516–1521.

13 M. ben Yahia, J. Vergnet, M. Saubanère and M. L. Doublet, *Nature Materials*, 2019, **18**, 496–502.

14 E. A. Olivetti, G. Ceder, G. G. Gaustad and X. Fu, *Joule*, 2017, **1**, 229–243.

15 X. Fu, D. N. Beatty, G. G. Gaustad, G. Ceder, R. Roth, R. E. Kirchain, M. Bustamante, C. Babbitt and E. A. Olivetti, *Environmental Science and Technology*, 2020, **54**, 2985–2993.

16 A. Abdellahi, A. Urban, S. Dacek and G. Ceder, *Chemistry of Materials*, 2016, **28**, 5373–5383.

17 H. Ji, D. A. Kitchaev, Z. Lun, H. Kim, E. Foley, D. H. Kwon, Y. Tian, M. Balasubramanian, M. Bianchini, Z. Cai, R. J. Clément, J. C. Kim and G. Ceder, *Chemistry of Materials*, 2019, **31**, 2431–2442.

18 R. J. Clément, D. Kitchaev, J. Lee and Gerbrand Ceder, *Chemistry of Materials*, 2018, **30**, 6945–6956.
19 D. H. Seo, J. Lee, A. Urban, R. Malik, S. Kang and G. Ceder, *Nature Chemistry*, 2016, **8**, 692–697.
20 G. Assat and J. M. Tarascon, *Nature Energy*, 2018, **3**, 373–386.
21 Z. Lun, B. Ouyang, D. A. Kitchaev, R. J. Clément, J. K. Papp, M. Balasubramanian, Y. Tian, T. Lei, T. Shi, B. D. McCloskey, J. Lee and G. Ceder, *Advanced Energy Materials*, 2018, **0**, 1802959.
22 Q. Jacquet, A. Iadecola, M. Saubanère, H. Li, E. J. Berg, G. Rousse, J. Cabana, M. L. Doublet and J. M. Tarascon, *Journal of the American Chemical Society*, 2019, **141**, 11452–11464.
23 D. A. Kuznetsov, B. Han, Y. Yu, R. R. Rao, J. Hwang, Y. Román-Leshkov and Y. Shao-Horn, *Joule*, 2018, **2**, 225–244.
24 J. Xu, M. Sun, R. Qiao, S. E. Renfrew, L. Ma, T. Wu, S. Hwang, D. Nordlund, D. Su, K. Amine, J. Lu, B. D. McCloskey, W. Yang and W. Tong, *Nature Communications*, 2018, **9**, 947.
25 R. Qiao, L. A. Wray, J. H. Kim, N. P. W. Pieczonka, S. J. Harris and W. Yang, *Journal of Physical Chemistry C*, 2015, **119**, 27228–27233.
26 K. Luo, M. R. Roberts, R. Hao, N. Guerrini, D. M. Pickup, Y. S. Liu, K. Edström, J. Guo, A. v. Chadwick, L. C. Duda and P. G. Bruce, *Nature Chemistry*, 2016, **8**, 684–691.
27 W. E. Gent, K. Lim, Y. Liang, Q. Li, T. Barnes, S. J. Ahn, K. H. Stone, M. McIntire, J. Hong, J. H. Song, Y. Li, A. Mehta, S. Ermon, T. Tyliszczak, D. Kilcoyne, D. Vine, J. H. Park, S. K. Doo, M. F. Toney, W. Yang, D. Prendergast and W. C. Chueh, *Nature Communications*, 2017, **8**, 2091.
28 Z. Zhuo, C. das Pemmaraju, J. Vinson, C. Jia, B. Moritz, I. Lee, S. Sallies, Q. Li, J. Wu, K. Dai, Y. de Chuang, Z. Hussain, F. Pan, T. P. Devereaux and W. Yang, *Journal of Physical Chemistry Letters*, 2018, **9**, 6378–6384.
29 U. Maitra, R. A. House, J. W. Somerville, N. Tapia-Ruiz, J. G. Lozano, N. Guerrini, R. Hao, K. Luo, L. Jin, M. A. Pérez-Osorio, F. Massel, D. M. Pickup, S. Ramos, X. Lu, D. E. McNally, A. v. Chadwick, F. Giustino, T. Schmitt, L. C. Duda, M. R. Roberts and P. G. Bruce, *Nature Chemistry*, 2018, **10**, 288–295.
30 K. Dai, J. Wu, Z. Zhuo, Q. Li, S. Sallis, J. Mao, G. Ai, C. Sun, Z. Li, W. E. Gent, W. C. Chueh, Y. de Chuang, R. Zeng, Z. xun Shen, F. Pan, S. Yan, L. F. J. Piper, Z. Hussain, G. Liu and W. Yang, *Joule*, 2019, **3**, 518–541.
31 G. Assat, D. Foix, C. Delacourt, A. Iadecola, R. Dedryvère and J.-M. Tarascon, *Nature Communications*, 2017, **8**, 2219.
32 G. Assat, A. Iadecola, C. Delacourt, R. Dedryvère and J. M. Tarascon, *Chemistry of Materials*, 2017, **29**, 9714–9724.
33 J. Lee, J. K. Papp, R. J. Clément, S. Sallis, D.-H. Kwon, T. Shi, W. Yang, B. D. McCloskey and G. Ceder, *Nature Communications*, 2017, **8**, 981.
34 S. E. Renfrew and B. D. McCloskey, *Journal of the American Chemical Society*, 2017, **139**, 17853–17860.
35 S. E. Renfrew and B. D. McCloskey, *ACS Applied Energy Materials*, 2019, **2**, 3762–3772.
36 S. E. Renfrew and B. D. McCloskey, *Journal of The Electrochemical Society*, 2019, **166**, A2762–A2768.
37 B. D. McCloskey, D. S. Bethune, R. M. Shelby, G. Girishkumar and A. C. Luntz, *The Journal of Physical Chemistry Letters*, 2011, **2**, 1161–1166.
38 B. D. McCloskey, R. Scheffler, A. Speidel, G. Girishkumar and A. C. Luntz, *Journal of Physical Chemistry C*, 2012, **116**, 23897–23905.
39 M. J. Crafton, Y. Yue, T.-Y. Huang, W. Tong and B. D. McCloskey, *Advanced Energy Materials*, 2020, **10**, 2001500.
40 S. Ramakrishnan, B. Park, J. Wu, W. Yang and B. D. McCloskey, *Journal of the American Chemical Society*, 2020, **142**, 8522–8531.
41 B. D. Mccloskey, A. Valery, A. C. Luntz, S. R. Gowda, G. M. Wallraff, J. M. Garcia, T. Mori and L. E. Krupp, *Journal of Physical Chemistry Letters*, 2013, **4**, 2989–2993.
42 R. Jung, M. Metzger, F. Maglia, C. Stinner and H. A. Gasteiger, *Journal of The Electrochemical Society*, 2017, **164**, A1361–A1377.
43 N. Mahne, S. E. Renfrew, B. D. McCloskey and S. A. Freunberger, *Angewandte Chemie - International Edition*, 2018, **57**, 5529–5533.
44 W. E. Gent, I. I. Abate, W. Yang, L. F. Nazar and W. C. Chueh, *Joule*, 2020, **4**, 1369–1397.
45 J. Hong, W. E. Gent, P. Xiao, K. Lim, D.-H. Seo, J. Wu, P. M. Csernica, C. J. Takacs, D. Nordlund, C.-J. Sun, K. H. Stone, D. Passarello, W. Yang, D. Prendergast, G. Ceder, M. F. Toney and W. C. Chueh, *Nature Materials*, 2019, **18**, 256–265.
46 K. A. Persson, B. Waldwick, P. Lazic and G. Ceder, *Physical Review B - Condensed Matter and Materials Physics*, 2012, **85**, 235438.
47 A. K. Singh, L. Zhou, A. Shinde, S. K. Suram, J. H. Montoya, D. Winston, J. M. Gregoire and K. A. Persson, *Chemistry of Materials*, 2017, **29**, 10159–10167.
48 J. Lee, D. H. Seo, M. Balasubramanian, N. Twu, X. Li and G. Ceder, *Energy and Environmental Science*, 2015, **8**, 3255–3265.
49 Z. Lun, B. Ouyang, Z. Cai, R. J. Clément, D.-H. Kwon, J. Huang, J. K. Papp, M. Balasubramanian, Y. Tian, B. D. McCloskey, H. Ji, H. Kim, D. A. Kitchaev and G. Ceder, *Chem*, 2019, 1–16.

